Large deformations of the hook affect free-swimming singly flagellated bacteria during flick motility

Mehdi Jabbarzadeh* and Henry Chien Fu
Department of Mechanical Engineering, University of Utah, Salt Lake City, Utah 84112, USA

(Received 24 July 2020; accepted 11 September 2020; published 29 September 2020)

Hook dynamics are important in the motility of singly flagellated bacteria during flick motility. Although the hook is relatively short, during reorientation events it may undergo large deformations, leading to nonlinear behavior. Here, we explore when these nonlinear and large deformations are important for the swimming dynamics in different ranges of hook flexibilities and flagellar motor torques. For this purpose, we investigate progressively more faithful models for the hook, starting with linear springs, then models that incorporate nonlinearities due to larger hook deformations. We also employ these models both with and without hydrodynamic interactions between the flagellum and cell body to test the importance of those hydrodynamic interactions. We show that for stiff hooks, bacteria swim with a flagellum rotating on-axis in orbits and hydrodynamic interactions between the cell body and flagellum change swimming speeds by about 40%. As the hook stiffness decreases, there is a critical hook stiffness that predicts the initiation of the dynamic instability causing flicks. We compare the transition value of stiffnesses predicted by our models to experiments and show that nonlinearity and large deflections do not significantly affect critical transition values, while hydrodynamic interactions can change transition values by up to 13%. Below the transition value, we observe precession of the flagellum, in which it deflects off-axis to undergo nearly circular stable trajectories. However, only slightly below the transition stiffness, nonlinearity in hook response destabilizes precession, leading to unstable deflections of the flagellum. We conclude that while the linear hook response can qualitatively predict transition stiffnesses, nonlinear models are necessary to capture the behavior of hooks for stiffnesses below transition. Furthermore, we show that for the lower range of hook stiffnesses observed in actual bacteria, models which capture the full deformations of hooks are necessary. Inclusion of the hydrodynamic interactions of the cell body, hook, and flagellum is required to quantitatively simulate nonlinear dynamics of soft hooks during flick motility.

DOI: 10.1103/PhysRevE.102.033115

I. INTRODUCTION

Flagellated bacteria swim by rotating helical flagellar filaments for propulsion. To power this rotation, a bacterial motor embedded in the cell body generates an almost constant torque for a wide range of rotational speeds [1–3]. This torque is transferred through a short flexible hook to the much stiffer rotating flagella [4–6]. For the flagellar filament, the bending stiffness is typically in the range of 1–10 pN μm^2, while for the hook, the bending stiffness varies widely between 0.0002–0.2 pN μm^2 for different species [4,6–8].

The elasticity of the hook is important in bacterial motility. The "run and tumble" motility of peritrichous bacteria requires the hook to bend to allow flagellar filaments to bundle and unbundle [9,10]. During a forward "run," multiple flagella—distributed around the cell surface and pointing in different directions—must orient together to form a bundle. For stable bundling, a certain stiffness and length of the hook are necessary [11]. If hooks are too stiff or too short, the flagella would not be able to orient together to form a bundle [8,11,12]. The "run-reverse-flick" motility of monotrichous bacteria requires the hook to bend during reorienting "flicks" [4,5,13]. A monotrichous bacterium alternates forward and backward runs by changing the rotation of its single flagellum at one pole from counterclockwise, with the flagellum pushing the cell, to clockwise, with the flagellum pulling the cell. During clockwise rotation of the flagellum, the hook unwinds and its stiffness decreases. Upon switching to counterclockwise rotation, the pushing flagellum places the unwound hook under compression and, after a short time, dynamical buckling instabilities of the hook cause the flagellum to make large deflections from the cell-body axis (a flick; Fig. 1) and reorient the entire bacterium [4,5,13]. During this process, the counterclockwise rotation winds the hook and increases its stiffness, and eventually it becomes stiff enough to stop buckling. Then, the bacteria runs forward in a straight trajectory with its flagellum on-axis. Thus, during preflick runs, the hook is unstable to large deflections, while during postflick runs, the hook is stable to large deflections.

To investigate the role of hook flexibility in different aspects of bacterial swimming dynamics, a number of different models have been used in previous studies. The swimming speed and stability of monotrichous bacteria [8], the instability of free-swimming multiflagellated bacteria to bundling [10,14,15], and the dynamics of spinning bacteria close to walls [16] have been studied by replacing the hook with a linear bending spring connecting the cell body to the flagella. The stiffness of the bending spring, k_b, is obtained from the bending stiffness EI and length L_H of the hook as

*jabbarzadeh.mehdi@utah.edu

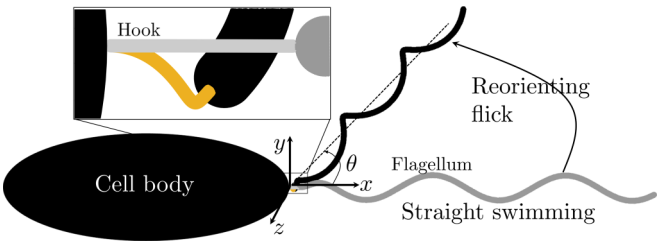

FIG. 1. A singly flagellated bacterium swims straight by rotating its flagellum straight behind the cell body, and reorients by a flick of its flagellum during which the flagellum undergoes large deflections (characterized by θ) associated with large nonlinear deformations of the hook.

$k_b = EI/L_H$. In our previous work [5] investigating flick motility, we showed that the hook also has an important torsional response, and modeled it as a combination of linear bending and torsional springs with stiffnesses calculated from the linearization of a Kirchhoff rod model. We showed that this simple model for hook bending, combined with a model for swimming dynamics that ignores hydrodynamic interactions between the flagellum, hook, and cell body, can predict the experimentally observed torques needed to initiate flicks.

It seems likely that for large bending, complex three-dimensional (3D) deformations (such as shown in Fig. 1) may become important. While simple linear spring models allow efficient computation and investigation for a wide range of cell body, flagellum, and hook parameters, linear models of hook response are not adequate for large hook deformations. Instead, Kirchoff rod models of the hook can be used to describe large hook deformations. Shum *et al.* investigated the dynamics of free-swimming singly flagellated bacterium, including the instability of straight swimming, by combining a Kirchoff rod model of the hook with a boundary element method to treat hydrodynamic interactions [17]. Park *et al.* [18] investigated the locomotion of singly flagellated bacteria during run-reverse-flick motility by modeling the flagellum and hook filaments as elastic, extensible Kirchoff rods, while describing hydrodynamic interactions by the method of regularized Stokeslets.

While with enough resolution (and computational cost) the approach of Shum *et al.* [17] can capture the full nonlinear behavior of the hook, it is still unclear which aspects of flick motility are dependent on the nonlinear large deformations of the hook, rather than the simple linear bending response that correctly predicts observed flick initiations [4,5]. In addition, for large deflections of the flagellum, the hydrodynamic interactions between the cell body and flagellum become more important in describing the swimmer's dynamics since the surfaces of the flagellum and cell body are close to each other. Previously, we have estimated that ignoring hydrodynamic interactions between the cell body and flagellum produces about 20% error in the swimming speed during runs, when deflections of the flagellum are small (i.e., stiff hooks and $\theta \sim 0$) [19–21], but errors could be significantly larger for large deflections of the flagellum (flexible hooks).

Here, we determine which aspects of flick motility are dependent on the effects of hook nonlinearity and large deformations, and what effects hydrodynamic interactions have on motility when there are large deflections of the flagellum. We do this by studying progressively more faithful models for the hook, starting with the previously employed (1) linear bending springs and (2) linear bending and torsional springs, then (3) models that incorporate nonlinearities due to larger hook deformations, (4) Kirchhoff rod models that fully incorporate large hook deformations, and, finally, a (5) numerical rod model that also incorporates the hydrodynamic interactions of the hook. We also employ models (1) through (4) both with and without hydrodynamic interactions between the flagellum and cell body to test the importance of those hydrodynamic interactions.

We show that for stiff hooks, a bacterium swims with its flagellum rotating on-axis. As the hook stiffness decreases, there is a transition to swimming in which the flagellum precesses about the axis with a large deflection angle θ (Fig. 1). The critical hook stiffness at which the transition occurs depends on the cell-body and flagellum geometry, hook model, and hydrodynamic interactions. For all hook stiffnesses below the critical value, linear spring models predict precession; however, for hook stiffnesses only slightly below the critical value, nonlinear effects destabilize precession into complex dynamics with large hook deformations. For these unstable deflections, we find that the choice of nonlinear models or Kirchoff rod models, as well as the inclusion of hydrodynamic interactions, can produce significantly different flagellum and cell-body trajectories. We demonstrate that for hook stiffnesses in the lower range of those observed biologically, large deformations occur during flicks. We conclude that while on-axis swimming and the destabilization of on-axis swimming can be understood using only the linear response of the hook, flick motility depends strongly on the nonlinear response of hooks undergoing large deformations.

II. METHODS

In this section, we first briefly review the inextensible Kirchoff rod model which can treat large deformations of thin filaments such as the hook. Then we discuss simplified linear and nonlinear parametrizations of the hook response which can be derived from the Kirchoff rod model. Finally, we discuss how to couple these models of the hook to swimming and deformation dynamics, including hydrodynamic interactions.

A. Inextensible kirchhoff rod models of the hook

Since the diameter of the hook is only 10 nm and its typical length is 100 nm, its elastic response can be treated as a slender inextensible Kirchhoff rod connecting the cell body to the flagellar filament, as described by Shum *et al.* [17]. During swimming, the surrounding fluid applies hydrodynamic forces and torques on the cell body, flagellum, and hook, but due to the short length of the hook, we ignore hydrodynamic forces on the hook itself.

We assume an initially straight and undeformed hook with length L_H and stiffness EI pointing along the x direction, that connects an ellipsoidal cell body to a helical flagellum. A molecular motor embedded in the cell body (body-hook junction) generates torques in the x direction in the

body-fixed frame and the hook transfers this torque to rotate the flagellum. The flagellum is at least two orders of magnitude stiffer than the hook for singly flagellated bacteria [4,6]. We treated the flexibility of the flagellar filaments before in our previous works [5,6], but here we assume rigid body motion of the flagellum and cell body in order to isolate the effects of the hook.

The Kirchhoff rod model treats the deformation of the hook by describing the position of the centerline of the hook as a curve in space, while tracking the orientation of cross sections of material along the centerline. Bending of the hook changes the orientation of material cross sections, producing elastic forces and moments. Due to the microscopic size of bacteria, they swim in the low Reynolds number regime, and at any time the hook's configuration and motion are such that force balance and moment balance are satisfied.

To study the hook's effects on the free-swimming dynamics of bacteria, we are interested in the displacements and orientations at the hook-flagellum junction due to the applied forces $\mathbf{F}_0$, torques $\mathbf{M}_0$ with components M_1, M_2, and M_3 in the x, y, and z direction, respectively, and motor rotational angle ϕ_M at the body-hook junction (Fig. 2). The orientation and position of the flagellum at the hook-flagellum junction are defined by polar angles $\boldsymbol{\alpha} = [\theta, \phi, \gamma]$ and displacement $\mathbf{X}$, respectively. The instantaneous orientation of the rigid flagellum $\hat{\mathbf{r}}$ is the same as the direction of the hook end point at the hook-flagellum junction $[\mathbf{d}_1(L_H)]$,

$$\hat{\mathbf{r}} = \mathbf{d}_1(L_H) = \cos(\theta)\hat{\mathbf{x}} + \sin(\theta)\cos(\phi)\hat{\mathbf{y}} + \sin(\theta)\sin(\phi)\hat{\mathbf{z}}, \quad (1)$$

in the local body-fixed frame. For constant motor torque $M_1 = M_M$, the Kirchhoff rod solutions can be summarized by defining vectorial input variables $\boldsymbol{\mathcal{X}} = [\phi_M, M_2, M_3, \mathbf{F}_0]$ and a nonlinear response function $\boldsymbol{\mathcal{G}}$ as

$$\begin{pmatrix} \boldsymbol{\alpha} \\ \mathbf{X} \end{pmatrix} = \boldsymbol{\mathcal{G}}(\boldsymbol{\mathcal{X}}; M_M). \quad (2)$$

The details of the Kirchhoff rod model and how Eq. (2) is computed are provided in Appendix A.

B. Simplified spring models of the hook

Here, we briefly describe simplified models of the hook that can be derived from the Kirchhoff rod model. These simplified models can include only the linear response or be extended to include some aspects of the nonlinear response.

The full description of the hook response in Eq. (2) relates applied forces and torques to the corresponding orientation and displacement of the flagellum. However, for small deflections, previous studies have simplified this to effective spring descriptions, for which it is assumed that since the displacement $\mathbf{X}$ is small compared to the swimmer length scale, most of the effects on the swimming dynamics come from the relative orientation of the flagellum with respect to the cell body [5,17]. The orientation of the flagellum (i.e., the end of the hook) is then related to the torques acting on the hook so the hook response is described by

$$\begin{pmatrix} \theta \\ \phi \end{pmatrix} = \boldsymbol{\mathcal{G}}_{\boldsymbol{m}}(M_\perp/M_M, \phi_T). \quad (3)$$

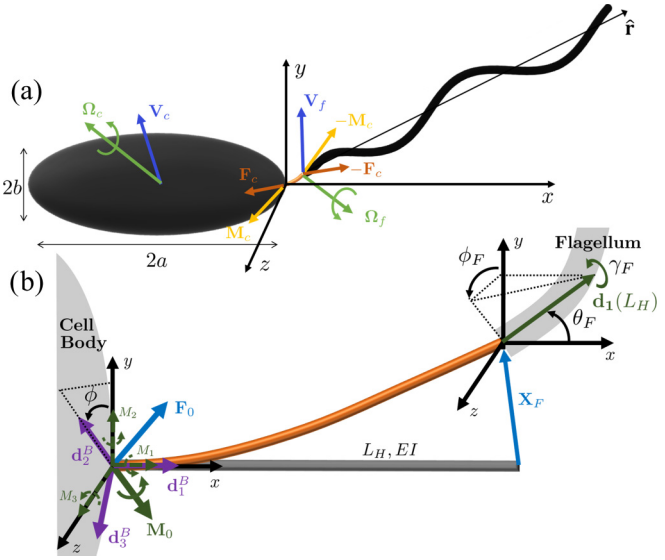

FIG. 2. Free-swimming model of singly flagellated bacteria. (a) A hook connects a rigid helical flagellum to an ellipsoidal cell body. The flagellar filament moves with translational and rotational velocities $(\mathbf{V}_F, \boldsymbol{\Omega}_F)$, respectively, and the cell body moves with translational and rotational velocities $(\mathbf{V}_c, \boldsymbol{\Omega}_c)$, respectively. The hook applies force $\mathbf{F}_c$ and torque $\mathbf{M}_c$ to the cell body at the body-hook junction, and equal and opposite force and torque to the flagellum at the flagellum-hook junction, to satisfy force- and torque-free conditions. (b) The bacterial motor embedded in the cell body at body-hook junction $x = 0$ generates a constant torque M_M in the x direction in the local body frame attached to the cell body. An orthonormal triad $\mathbf{d}_1^B, \mathbf{d}_2^B, \mathbf{d}_3^B$ following the material of the hook is defined at the body-hook junction $(x = 0, s = 0)$; $\mathbf{d}_1^B$ is always in the x direction and $(\mathbf{d}_2^B, \mathbf{d}_3^B)$ rotate along with the motor rotor by an angle ϕ_M along the x axis. The hook is initially undeformed and straight along the x direction. During swimming, applied forces and torques deform it so that the tangent direction at the hook-flagellum junction, and hence the rigid flagellum orientation, is $\mathbf{d}_1(L_H)$, described by angles (θ, ϕ, γ) via Eq. (1).

Note that by symmetry, θ and ϕ do not depend on ϕ_M. In addition, by dimensional analysis, we can rewrite the components of the moment in terms of $M_\perp = \sqrt{M_2^2 + M_3^2}$, the magnitude of applied perpendicular torques, normalized by motor torque M_M, and ϕ_T, the angle that the perpendicular torque applied on the hook makes with the z direction, with a positive angle tending toward the negative y direction [5].

The simplest and most computationally efficient approaches are linear models in which the hook is replaced by a linear spring. Here, we study two different linear models, i.e., a linear bending spring, and a linear bending and torsional spring. In the linear bending spring model, the hook deflection angle θ is a linear function of the applied torque ratio $M_\perp/M_M$, so Eq. (3) becomes

$$\theta = \frac{1}{k_H}\left|\frac{M_\perp}{M_M}\right|, \quad (4)$$

where the spring constant $k_H = EI/(L_H M_M)$ depends on the bending stiffness EI, length L_H of the hook, and motor torque

M_M. For a pure bending spring, $\phi = \phi_T$, i.e., the hook bends in a direction perpendicular to the applied torque.

In the linear bending and torsional spring model, we take into account the fact that when subjected to both the applied torque ($M_\perp$) and the motor torque, the hook not only bends, but also twists. This corresponds to including changes in both θ and $\phi - \phi_T$ at the flagellar end of the hook. In this approach, the polar coordinates can be linearly related to the applied torque as

$$\begin{pmatrix} \theta \\ \phi - \phi_T \end{pmatrix} = \begin{pmatrix} \alpha_\theta(k_H) \\ \alpha_\phi(k_H) \end{pmatrix} \left| \frac{M_\perp}{M_M} \right| + \begin{pmatrix} 0 \\ \beta_\phi(k_H) \end{pmatrix}, \tag{5}$$

where $(\alpha_\theta, \alpha_\phi, \beta_\phi)$ are parameters which are functions of nondimensional hook parameter $k_H = EI/(L_H M_M)$ (see Appendix B).

The linearized springs fail to capture nonlinearities in the hook response for small stiffnesses or large loads acting on the filament. To add nonlinear effects, we can use nonlinear bending and torsional spring models with spring coefficients that are also functions of the applied torques, $M_\perp/M_M$. Specifically, we use a cubic interpolation to fit the hook behavior such that

$$\begin{pmatrix} \theta \\ \phi - \phi_T \end{pmatrix} = \begin{pmatrix} \alpha'_\theta \\ \alpha'_\phi \end{pmatrix} \left| \frac{M_\perp}{M_M} \right|^3 + \begin{pmatrix} \beta'_\theta \\ \beta'_\phi \end{pmatrix} \left| \frac{M_\perp}{M_M} \right|^2 + \begin{pmatrix} \gamma'_\theta \\ \gamma'_\phi \end{pmatrix} \left| \frac{M_\perp}{M_M} \right| + \begin{pmatrix} 0 \\ \delta_\phi \end{pmatrix}. \tag{6}$$

The details of this model and comparisons between the linear spring, nonlinear spring, and Kirchhoff rod response are described in Appendix B.

C. Swimming dynamics of a singly flagellated bacterium

For a free-swimming bacterium, the force- and torque-free conditions require that if a force $\mathbf{F}_c$ and torque $\mathbf{M}_c$ are exerted on the cell body by the hook, then $-\mathbf{F}_c$ and $-\mathbf{M}_c$ are exerted on the flagellum by the hook, as shown in Fig. 2(a). To solve for the swimming dynamics using the full Kirchhoff rod model [Eq. (2)], we start from a known initial condition of forces and torques, $(\mathbf{F}_c, \mathbf{M}_c) = (\mathbf{0}, M_M \hat{\mathbf{x}})$ at $t = 0$, and we need to determine the translational and rotational velocities of the cell body $(\boldsymbol{V}_c, \boldsymbol{\Omega}_c)$ as well as the translational and rotation velocities of the flagellum $(\boldsymbol{V}_f, \boldsymbol{\Omega}_f)$. In the low Reynolds number limit and assuming rigid body motion for the cell body and flagellum, we have

$$\begin{pmatrix} \mathbf{F}_c \\ \mathbf{M}_c \\ -\mathbf{F}_c \\ -\mathbf{M}_c \end{pmatrix} = \mathbf{R} \begin{pmatrix} \boldsymbol{V}_c \\ \boldsymbol{\Omega}_c \\ \boldsymbol{V}_f \\ \boldsymbol{\Omega}_f \end{pmatrix}, \tag{7}$$

where $\mathbf{R} = [\mathbf{R}_{cc}, \mathbf{R}_{cf}; \mathbf{R}_{fc}, \mathbf{R}_{ff}]$ is the joint resistance matrix of the cell body and flagellum. It can be computed including all hydrodynamic interactions between the cell body and flagellum, or we can ignore the hydrodynamic interactions between the cell body and flagellum by isolating the cell body and flagellum to calculate the resistance matrix $\mathbf{R}_{cc}$ (resistance matrix of the cell body) and $\mathbf{R}_{ff}$ (resistance matrix of the flagellum), while the off-diagonal blocks are zero ($\mathbf{R}_{fc} = \mathbf{R}_{cf} = \mathbf{0}$). The resistance matrices are calculated using our previously reported implementation [19,22–25] of the method of regularized Stokeslets [26,27]. The relative velocities of the cell body and flagellum determine the rate of change of the displacement vector $\dot{\mathbf{X}} = \boldsymbol{V}_f - \boldsymbol{V}_c$ and the relative angular velocity $\boldsymbol{\Omega} = \boldsymbol{\Omega}_f - \boldsymbol{\Omega}_c$, while the geometric constraint $\dot{\hat{\mathbf{r}}} = \boldsymbol{\Omega} \times \hat{\mathbf{r}}$ determines the rates of changes of the polar coordinates $\boldsymbol{\alpha}$ [$\dot{\boldsymbol{\alpha}} = [\dot{\theta}, \dot{\phi}, \dot{\gamma}]$; Fig. 2(b)],

$$\begin{aligned} \dot{\theta} &= \Omega_z \cos(\phi) - \Omega_y \sin(\phi), \\ \dot{\phi} &= \Omega_x - \cot(\theta)[\Omega_y \cos(\phi) + \Omega_z \sin(\phi)], \\ \dot{\gamma} &= \Omega_x - \tan(\theta/2)[\Omega_y \cos(\phi) + \Omega_z \sin(\phi)], \end{aligned} \tag{8}$$

where $\dot{\gamma}$ is the rotation rate of the flagellar filament along its centerline axis. Taking the time derivative of Eq. (2),

$$\frac{d}{dt} \begin{pmatrix} \boldsymbol{\alpha} \\ \mathbf{X} \end{pmatrix} = \frac{\partial \mathcal{G}}{\partial \boldsymbol{\mathcal{X}}} \dot{\boldsymbol{\mathcal{X}}}. \tag{9}$$

The partial derivative $\frac{\partial \mathcal{G}}{\partial \boldsymbol{\mathcal{X}}}$ can be evaluated using a finite difference approach at each time step for known forces and torques ($\boldsymbol{\mathcal{X}}$) [17]. From $\dot{\mathbf{X}}$, $\dot{\boldsymbol{\alpha}}$, and Eq. (9), we determine the rate of changes of forces, torques, and motor rotation ($\dot{\boldsymbol{\mathcal{X}}}$), which are integrated in time to obtain $\boldsymbol{\mathcal{X}}$. The trajectory of the flagellum is obtained by integrating $\dot{\boldsymbol{\alpha}}$ in time.

To solve for the swimming dynamics for the simplified spring models, in which only the torques are known from configuration of the flagellum [Eqs. (4)–(6)], we use Eq. (7), but since the hook displacement is constant in these models, the cell body and flagellum have the same velocity, $\boldsymbol{V}_c = \boldsymbol{V}_f = \boldsymbol{V}$. Then, Eq. (7) gives 12 linear equations which can be solved for the 12 unknown components of $\boldsymbol{V}$, $\boldsymbol{\Omega}_c$, $\boldsymbol{\Omega}_f$, and $\mathbf{F}_c$ in the body-fixed frame. To track the trajectory of the flagellum specified by polar coordinates $\boldsymbol{\alpha}$, we calculate their rates of changes given by Eq. (8). We numerically integrate $\dot{\boldsymbol{\alpha}}$ in time to obtain the trajectory of the flagellum orientation.

D. Numerical inextensible rod model

In the Kirchhoff rod model described in Sec. II A, the hydrodynamic interactions of the slender hook with the surrounding fluid are considered to be negligible due to its short length and small diameter. In general, one may be interested in a more accurate model that includes hydrodynamic interactions of the hook by discretizing the hook into small segments of length Δs. The ratio of the timescale (τ_s) needed to resolve the stretching dynamics of the hook to the timescale (τ_b) needed to resolve the bending dynamics of the hook is $\tau_s/\tau_b = EI/(EA\Delta s^2)$ [6]. Since the typical diameter of the hook is only 10 nm and we use fine discretization scales $\Delta s/d = 2$ to capture nonlinear deformations of the hook, this ratio is $\tau_s/\tau_b \sim 0.01$, implying that extension of the hook is much stiffer than bending. Thus the hook can be well approximated as an inextensible filament [6]. We have developed a numerical method, which discretizes inextensible Kirchhoff rods moving in viscous fluids [6], appropriate for the large deformations we study here.

Briefly (see Appendix C and Ref. [6] for details), in this model the centerline of the hook is discretized into straight cylindrical segments. For each segment, two different kinds of forces and torques can be considered. External forces and torques exerted on the segment by the surrounding fluid through its surface are related to the motion of the cell body,

TABLE I. Dimensions of the flagellar filament and cell body for *V. alginolyticus* [4,5].

Flagellar filament					Hook				Cell body	
Flagellar pitch P (μm)	Filament radius r (μm)	Helix radius R (μm)	Contour length L (μm)	Axial length L_x (μm)	Filament diameter d_H (μm)	Length L_H (μm)	Relaxed bending stiffness EI (pN μm^2)	Loaded bending stiffness EI_w (pN μm^2)	Head length $2a$ (μm)	Head width $2b$ (μm)
1.49	0.016	0.14	4.59	3.97	0.01	0.1	0.036	0.22	3.2	1.2

hook, and flagellum by a boundary element method for Stokes equations [6], while internal forces and torques exerted on the segment by neighboring segments through cross sections of the filament are calculated from the Kirchhoff rod model. Net force and torque balance on each segment allows us to solve for the translational and rotational velocities of all segments. Integrating these velocities in time describes the displacement and orientation of the segments and hence the evolution of the deformed shape of the hook filament, as well as the motion of the cell body and flagellum.

E. Geometries and parameters

For numerical simulations, we use an ellipsoidal cell body with major and minor axis of $2a$ and $2b$, respectively. A tapered helical flagellar filament with filament radius of r, helical radius R, and helical pitch P is attached to the hook and is initially placed along the x direction, with its centerline described by [5,18,20–22]

$$\mathbf{r}_c(s) = (s + L_H)\hat{\mathbf{x}} + R(1 - e^{-(\frac{2\pi s}{P})^2})\left[\cos\left(\frac{2\pi s}{P}\right)\hat{\mathbf{y}} + \sin\left(\frac{2\pi s}{P}\right)\hat{\mathbf{z}}\right], \tag{10}$$

where L_H is the length of the hook and s varies between zero and flagellum axial length L_x ($s \in [0, L_x]$). The numerical values for the geometry of the cell body and flagellar filament are given in Table I. The motor is placed at $x = 0$, generating constant counterclockwise (viewed from behind the cell body) torque M_M applied to the base of the hook. Deformation of the hook changes the position and orientation of the rigid flagellar filament over time according to Eq. (1).

III. RESULTS

Here, we first describe the qualitative flagellar behaviors predicted by our models as hook stiffness varies. Then we describe how the predicted behaviors change as different physical effects are included in our models, which indicates which physical effects are responsible for each behavior.

A. Flagellar orbits, stable precession, and unstable deflections

We calculate the trajectory of flagellum orientation (θ, ϕ) during bacterial free swimming. We trace the instantaneous centerline orientation $\hat{\mathbf{r}}$ [Eq. (1)] of the flagellum over time. We characterize the swimming dynamics by the steady-state trajectory of the flagellum in the body-fixed frame. Depending on the model used for the simulation and stiffness of the hook, we observe three general types of dynamics described in detail below: orbits, precession, and unstable deflections.

For the stiffest hooks (largest k_H), the centerline of the flagellum moves around $\hat{\mathbf{x}}$ such that the end point of the centerline nearly traces a circular orbit [Fig. 3(a)]. The deflection angle θ is small [plotted in Fig. 3(d)], meaning that the flagellum makes very small deviations from its initial orientation. One orbit of the end point occurs for each motor revolution. These stable orbits correspond to nearly straight trajectories of the cell body, as discussed in previous studies [5,8,17,18,22].

As the hook stiffness decreases below a critical value k_H^*, the behavior transitions from small orbits to large precession. During precession, typical deflection angles θ are much larger than orbits and the radius of precession is comparable to the swimmer's length scale [Fig. 4(b)], but the flagellum still traces a nearly circular trajectory around the central $\hat{\mathbf{x}}$ direction. In precession, one revolution of the flagellar tip requires multiple motor rotations; each motor rotation is one wiggle of the trajectory shown in Fig. 3(b). Precession has been previously reported for linear models of the hook and corresponds to helical trajectories of the cell body [5,8,16].

For even smaller hook stiffnesses, some models transition to unstable deflections, in which the deflection angle of the flagellum increases without saturating, as shown in Fig. 3(c). Unstable deflections have previously been seen in full rod models of the hook [17,18,28] and may correspond to three-dimensional reorienting trajectories of the cell body for both rigid [17] and flexible [18] flagella.

To differentiate stable precession from unstable deflections, we plot the deflection angle θ as a function of motor revolution ϕ_m (which increases monotonically as time increases) as in Fig. 3(d). In Fig. 3(d), we use examples computed using the linearized and full models for a hook parameter $k_H = 0.5$ slightly below the critical value $k_H^* = 0.57$. For the linearized model, after a transient (for $\phi_m > 500$), the deflection angle θ oscillates around 27°, representing precession. In contrast, for the full Kirchhoff rod model, we observe unstable deflections: the angle θ increases without saturating; we stop the simulation when the flagellum hits the cell body (at $\theta \approx 80°$).

To compare different models, we plot the steady-state deflection angle of the flagellum as a function of hook stiffness k_H in Fig. 4. For unstable deflections, we plot a vertical line. For stiff hooks ($k_H > k_H^*$), all the models predict a stable orbit, but k_H^* differs for the different models. For less stiff hooks or greater motor torques ($k_H < k_H^*$), orbits become unstable and instead the flagellum precesses [Fig. 3(b)]. For the linear spring models, precession occurs for all $k_H < k_H^*$. For the nonlinear spring model, Kirchoff rod model, and numerical inextensible models, there is a small range right below the critical values ($0.98 < k_H/k_H^* < 1$) where precession is observed, but for smaller k_H, unstable deflections are observed instead. Table II summarizes the behavior of different models

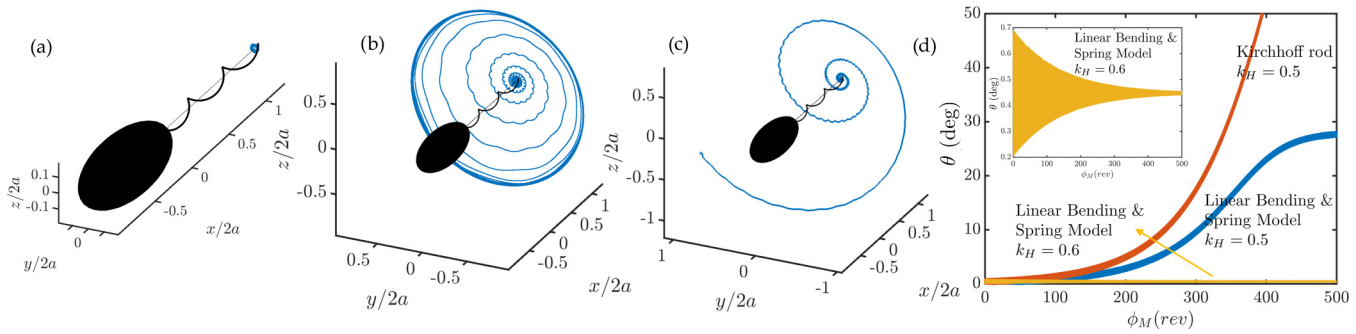

FIG. 3. Examples of flagellar trajectories relative to the cell body for orbits, stable precession, and unstable deflections generated using the Kirchhoff rod model. The end of the flagellum traces a nearly circular trajectory (blue-dashed line) for (a) small orbits with $k_H > k_H^*$ and (b) large precession with $0.98 < k_H^*/k_H < 1$ during free swimming. (c) The flagellum orientation traces unstable deflections for softer hooks, $k_H < 0.98k_H^*$. The motor torque is $M_M = 2$ pN μm for these simulations. (d) The corresponding instantaneous deflection angle θ is plotted as a function of motor revolution ϕ_M for orbits (yellow line: $k_H = 0.6 > k_H^*$) and precession (blue line: $k_H = 0.5 < k_H^*$) for the linearized bending and torsional spring model. The deflection angle increases without saturating for unstable deflections obtained from the full Kirchhoff rod model (orange line).

for small ($k_H < k_H^*$) and large ($k_H > k_H^*$) hook stiffnesses. The different models incorporate different physical effects, so below we use the differences in predicted behaviors to determine the importance of those physical effects in causing these behaviors.

B. Transition from small orbits to large deflections—comparison to experiments

The critical hook parameter k_H^* defines the transition from small orbits to precession. k_H^* depends on the geometries of the cell body and flagellum, motor torque, and hook stiffness (since $k_H = EI/M_M L_H$). Here, since we use the same geometry (Table I) for all simulations, the different values of k_H^* in Fig. 4 are due to the different physical effects considered in this study. The smallest critical value ($k_H^* \approx 0.41$) is predicted by the linear bending spring. The linearized hook response (linear bending and torsional spring), nonlinear bending and torsional spring, and the full Kirchoff rod model predict the same critical value $k_H^* \approx 0.57$ (all neglecting hydrodynamic interaction between the cell body and flagellum). This is reasonable since the stability of orbits can be calculated while deflections remain small, and so all these models effectively behave in the linear regime. Including hydrodynamic interactions between the cell body and flagellum increases the critical transition values by about 10% to $k_H^* \approx 0.63$ (only the linearized model with hydrodynamic interactions is shown by the black curve in Fig. 4). Including the hydrodynamic interactions of the hook as well (numerical inextensible model) predicts $k_H^* \approx 0.65$, only 3% larger than the value without the hydrodynamic effects of the hook.

Flicks are initiated by the dynamic buckling instability when $k_H = EI/M_M L_H < k_H^*$ [5]. For each model mentioned above, the critical k_H^* depends on body and flagellum geometry. We compare the predictions of different models with previously reported experimentally observed runs [4,5]. In these experimental runs, the cell-body geometry and the swimming speed were reported for 54 preflick and 21 postflick runs of different cells of *Vibrio alginolyticus* [4]. Experimentally, it is observed that the preflick runs have an unwound hook (with small bending stiffness EI_u; see Table I) and are unstable to a flick deformation of the hook, while the postflick runs have a wound hook (with large bending stiffness EI_w; see Table I) and are stable to flick deformations. In our previous paper [5], we calculated $k_H = EI/(M_M L_H)$ for each run, by evaluating the motor torque M_M for free-swimming cells by matching the measured swimming speed for each cell-body geometry to the value calculated using the method of regularized Stokeslets [5]. The value of EI is chosen to be EI_u or EI_w for pre- or postflick runs, respectively, while L_H is given

TABLE II. Behavior of different models for varying hook stiffnesses in the biologically relevant range $0.18 < k_H < 1.1$.

	Linear bending spring	Linear bending and torsional spring	Nonlinear bending and torsional spring	Full Kirchhoff rod model	Numerical inextensible model
Orbit	$k_H > k_H^*$	$k_H > k_H^*$	$k_H > k_H^*$	$k_H > k_H^*$	$k_H > k_H^*$
Critical k_H^*	$0.26 < k_H^* < 0.41$	$0.46 < k_H^* < 0.57$	$0.46 < k_H^* < 0.57$	$0.46 < k_H^* < 0.57$	$0.58 < k_H^* < 0.73$
Precession	$k_H < k_H^*$	$k_H < k_H^*$	$0.98 < k_H/k_H^* < 1$	$0.98 < k_H/k_H^* < 1$	$0.98 < k_H/k_H^* < 1$
Unstable deflections	Not observed in validity range	Not observed in validity range	$k_H < 0.98k_H^*$	$k_H < 0.98k_H^*$	$k_H < 0.98k_H^*$
Validity for k_H	Accurate for $k_H > 0.6$	Accurate for $k_H > k_H^*$	Accurate for $k_H > 0.4$	Accurate	Accurate
Hook hydrodynamics	Not included	Not included	Not included	Not included	Included

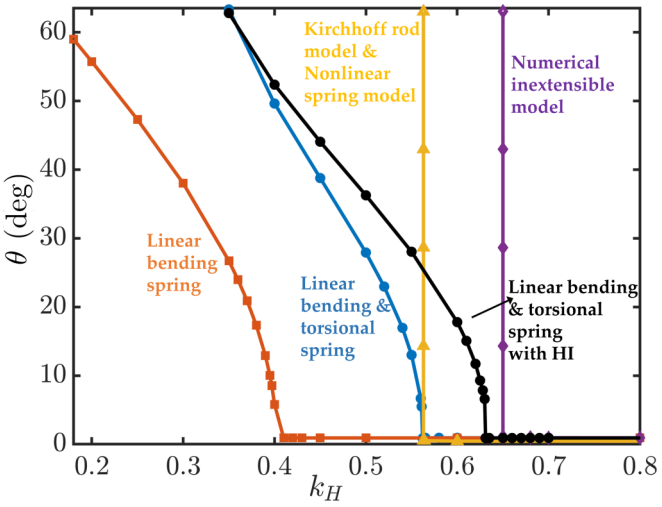

FIG. 4. Steady-state deflection angle θ of the flagellum for different hook stiffness parameters k_H. Unstable deflection of the flagellum cannot be characterized by steady-state motions and are represented by vertical lines. The simple bending spring model (squares, orange) predicts the smallest critical values of $k_H^* = 0.41$ for the destabilization of orbits. The linearized bending and torsional spring (circles, blue), nonlinear spring, and full rod model without hydrodynamic interactions (triangles, yellow) give the same critical value $k_H^* = 0.57$. Hydrodynamic interactions between body and flagellum change critical values by about 10% for the linearized bending and torsional spring (circles, black). The numerical inextensible model of the hook including hydrodynamic interactions of the hook, cell body, and flagellum predicts $k_H^* = 0.65$.

in Table I. The value of $1/k_H$ for each run is plotted in Fig. 5. Then, for each model used in this paper, we calculate the range of k_H^* from the different cell-body geometries, assuming the same flagellum parameters (Table I) for all different cells. Thus, for each model, we obtain a range of critical parameters

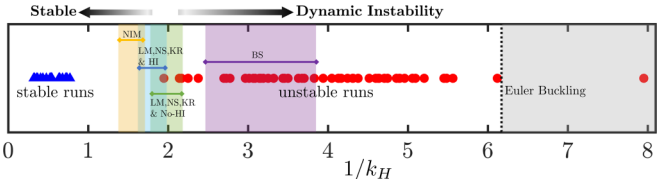

FIG. 5. Calculated $1/k_H$ values of stable runs (blue triangles) should lie in the stable regime to the left of the critical values predicted by the dynamic buckling instability from different models, while those of dynamically unstable runs (red circles) should lie to the right of the predicted critical values. Nearly all unstable runs do not exceed the static Euler buckling criterion (solid line). Each colored region is the range of critical values calculated for different experimental bacterial geometries by the labeled set of models. The linear bending spring (BS, purple) does not predict about half of the preflick runs. The numerical inextensible model (NIM, yellow) accurately describes all observed runs. The linear bending and torsional spring (LM), nonlinear bending and torsional spring (NS), and full Kirchhoff rod (KR) models without hydrodynamic interactions (all the same green band) predict all but three preflick runs correctly, while with hydrodynamic interactions (turquoise band), they predict all but one preflick run correctly.

k_H^*, which is the range reported in the second row of Table II. In Fig. 5, we also plot the range of $1/k_H^*$ predicted by each model as vertical bands of different colors.

Comparing the $1/k_H$ values of the runs to the calculated critical values, we expect that the stable postflick runs should be to the left of the $1/k_H^*$ bands, while the unstable preflick runs should be to the right of the $1/k_H^*$ band. The vertical black line is the critical $1/k_H^*$ corresponding to the static Euler buckling criterion [5]; since most of the dynamically unstable preflick runs (red circles) are to the left of the criterion, it does not predict flick initiation well. The simple bending spring model (purple band) predicts only about half of preflick runs correctly, while the linear bending and torsional spring, nonlinear bending and torsional spring, and full Kirchhoff rod model (green band, all without hydrodynamic interactions of the cell body and flagellum) predict all but three preflick runs correctly. Adding cell body and flagellum hydrodynamic interactions to these models (turquoise band) makes them even more accurate, and they predict all but one of the experimental preflick runs correctly. Finally, including hydrodynamic interactions of the hook (yellow band, the numerical inextensible model) accurately predicts all preflick runs.

C. Transition to unstable deflections

While the linear spring models predict precession for all $k_H < k_H^*$, the nonlinear springs, full Kirchoff rod, and numerical inextensible models all predict that precession only occurs for $0.98 < k_H/k_H^* < 1$, and for smaller k_H, unstable deflections are observed. Thus nonlinearity is sufficient to destabilize precession for most k_H, and linear models are not adequate to describe the flagellum dynamics even qualitatively. Note that (as indicated in Table II and discussed in the next section) the nonlinear bending and torsional spring is also not accurate for very flexible hooks ($k_H < 0.4$).

To understand the deficiency of the linearized model, we first compare the hook response of the linear bending and torsional spring, nonlinear bending and torsional spring, and full Kirchoff rod, for $k_H = 0.5$ (slightly below k_H^*), at which the linear model predicts precession but the other models predict unstable deflections. We generate a trajectory using the full Kirchhoff rod model by applying constant motor torque M_M and calculate the polar angles (θ, ϕ), as well as the perpendicular torque $M_\perp$, and torque angle ϕ_T as a function of time. The black curves in Figs. 6(a) and 6(b) show these results for the full Kirchoff rod model. Then, for each set of angles (θ, ϕ, ϕ_T) of this trajectory, we also find the perpendicular torque in the linearized and nonlinear bending and torsional spring models [Eqs. (5) and (6), respectively), and plot those as the blue and orange curves, respectively, in Figs. 6(a) and 6(b). By comparing the curves in Fig. 6(a), we see that the response of the deflection angle θ for all three models is quite similar, with differences of less than 5%, but the actual twisting angle $\phi - \phi_T$ response is quite nonlinear. Including nonlinearity as in the nonlinear spring model seems to be enough to destabilize precession.

Nonetheless, it is also evident from Fig. 6(b) that the twisting response of the nonlinear spring is still quite different from that of the full Kirchhoff rod model, especially at small $M_\perp/M_M$. To understand the origin of this difference, note

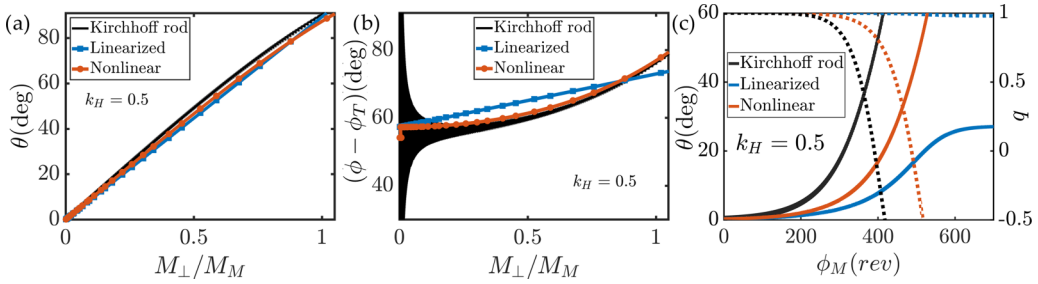

FIG. 6. Accuracy of the linear (blue) and nonlinear (orange) bending and torsional spring models for flagellum deflections and swimming directions at $k_H = 0.5$. (a),(b) The deflection angles (θ, ϕ) are compared to the exact response of the hook (Kirchoff rod model, black) as a function of applied torque ratios. (c) The instantaneous deflection angle θ is plotted as a function of motor revolution ϕ_m for trajectories generated by the linear bending and torsional spring (blue line), nonlinear bending and torsional spring (orange line), and full Kirchhoff rod model (black line). The linearized model predicts stable precession with deflection angle of about 27°. The nonlinear spring and full Kirchoff rod models predict unstable deflections, but with different trajectories of the cell body as identified by the alignment parameter $q = (\mathbf{V}_c \cdot \hat{\mathbf{x}})/|\mathbf{V}_c|$, where $\mathbf{V}_c$ is the velocity of the cell body in the fixed laboratory frame (dashed lines and right axes).

that the spring models were obtained by assuming a typical axial force in the x direction of 1 pN μm and ignoring any perpendicular forces. On the other hand, the full Kirchhoff rod model includes force and displacement effects given by Eq. (2). Ignoring the effects of perpendicular forces in the nonlinear spring yields a monotonic response of the twisting angle [orange curve in Fig. 6(b)], while the fluctuations of the twisting angle in the Kirchhoff rod model (black curve) are due to the force effects (black line). These fluctuations are most significant for small applied torques $M_\perp/M_M < 0.2$, while torque effects dominate for larger applied torques and large deflections.

While the nonlinear spring ignoring the force effects does produce the correct qualitative behavior of unstable deflections, due to the differences with the full Kirchhoff model, it does not produce quantitatively accurate trajectories. In Fig. 6(c), we plot the deflection angle θ and the alignment parameter $q = (\mathbf{V}_c \cdot \hat{\mathbf{x}})/|\mathbf{V}_c|$ ($\mathbf{V}_c$ is the velocity of the cell body in the fixed laboratory frame) between the cell-body axis and the x direction as a function of motor revolution during trajectories generated by the linear bending and torsional spring model, nonlinear spring model, and full Kirchhoff model. In all cases, $k_H = 0.5$, as in Figs. 6(a) and 6(b). Both the nonlinear and full Kirchhoff models show deflection angles corresponding to unstable deflection, but their deflection and alignment parameter are quite different quantitatively.

D. Very flexible hooks and large deformations

To determine when large deformations of the hook start to become important, we consider the entire range of hook stiffnesses measured during run-reverse-flick motility, which due to winding and unwinding of the hook can be quite large. For *Vibrio*, this range is measured to be $0.18 < k_H < 1.1$, for which the smallest and largest values correspond to the unwound and wound states of the hooks, respectively [4,5]. At the small unwound hook stiffness, we expect the hook response (and hence the swimming dynamics) to be very sensitive to the applied forces and torques, and show complex and large deformations.

To investigate the hook's response and deflections for a range of stiffnesses, we show the hook shapes and deformations alongside plots of the deflection and twisting angles as a function of applied torques for different k_H in Fig. 7. For stiffer hooks ($k_H > 0.4$), the hook end orientations (θ, ϕ) are monotonic functions of the applied torque $M_\perp/M_M$, and hook deflections can be approximated by a simple cantilever beam under small loads. On the other hand, for less stiff hooks ($k_H < 0.4$), the hook end orientations are highly nonlinear and the deformations are complex 3D curves. This nonlinearity in θ is significant enough to make $M_\perp/M_M$ a multivalued function of θ [the yellow and purple curves of Fig. 7(a)], which cannot be captured using a single-valued nonlinear spring model. Thus, to study the dynamics of hook in this lower range of stiffnesses, large and complex deformations need to be accounted for, as is possible with either the full Kirchhoff rod model or the numerical inextensible model.

E. Effect of hydrodynamic interactions on hook dynamics

The effects of hydrodynamic interactions between the cell body, flagellum, and hook on the critical transition value k_H^* was discussed in Sec. III B. We showed that including hydrodynamic interactions between the cell body and flagellum modifies k_H^* by about 10%, and including hydrodynamic interactions with the hook modified k_H^* by only 3%. These relatively small effects on the destabilization of orbits reflect the fact that during orbits, the hook remains almost straight with small deflection angles, so the flagellum stays far from the cell body.

However, for the large deflections observed during precession and unstable deflections, the flagellum is closer to the surface of the cell body and we expect significant hydrodynamic interactions between the cell body and flagellum that can affect the swimming dynamics of bacteria. To see the effect of hydrodynamic interactions between the cell body and flagellum on swimming velocities, we take the trajectory used in Fig. 6, which was generated using the full Kirchhoff rod model for $k_H = 0.5$ without hydrodynamic interactions, and plot V_x, the velocity along the swimming direction, and Ω_x, the cell-body angular velocity about the swimming direction, as a function of deflection angle in Figs. 8(a) and 8(b). Then, at each time, we also compute these velocities including hydrodynamic interactions for each configuration in the trajectory

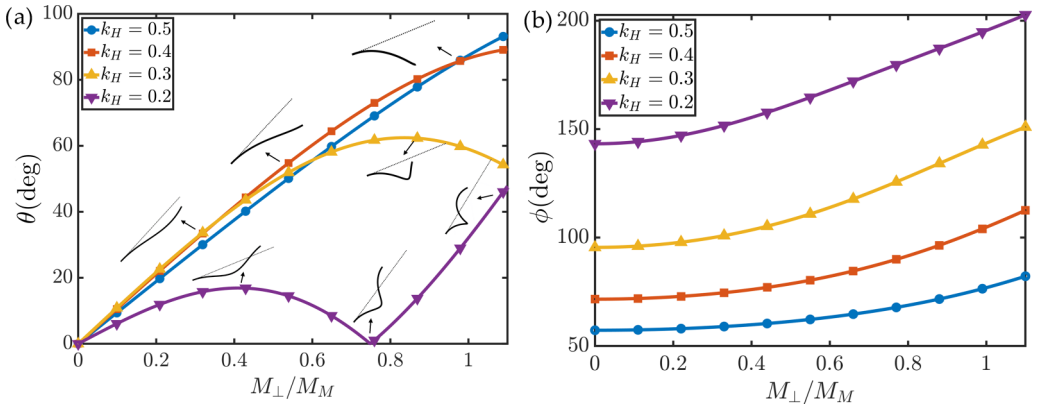

FIG. 7. Large and nonlinear deformations of soft hooks. (a) The deflection angle θ is shown for varying hook stiffness as a function of applied torque ratio $M_\perp/M_M$. For $k_H < 0.4$, θ is not a monotonic function of applied torque ratios, and for $k_H = 0.2$, its behavior is highly nonlinear. The shapes of the deformed hook are plotted alongside each curve; nonmonotonic behavior is correlated with large complex deformations. (b) The deflection angle ϕ is shown as a function of applied torque ratio.

that was generated without hydrodynamic interactions. Note that the force and torque on the cell body and flagellum are the same with and without hydrodynamic interactions since they are determined by the motor torque and hook shape (via the Kirchhoff rod model). Including hydrodynamic interactions of the cell body and flagellum, the swimming speeds are decreased by about 38% for small deflections ($\theta < 1$), and can change by up to 80% for large deflections. The effect of hydrodynamic interactions on the rotation rate of the ellipsoidal cell body is about 5% for small deflections and 10% for larger deflections, as plotted in Fig. 8(b). We plot the difference in velocities, ΔV, between velocities calculated with and without hydrodynamic interactions in Fig. 8(c), from which it can be seen that hydrodynamic interactions produce even greater changes in the other components of the swimming velocity (V_y, V_z).

The results shown in Fig. 8 isolate the effect of hydrodynamic interactions on velocities, but since the velocities change, including hydrodynamic interactions also changes the entire trajectory of hook deformations, flagellum orientations, and the cell body. To show how hydrodynamic interactions change the trajectories, we generate separate trajectories using the full Kirchoff rod model with and without hydrodynamic interactions for $k_H = 0.5$, and plot the hook deflection angle θ and cell-body alignment parameter q as a function of motor revolution in Fig. 9. While both trajectories have similar deflection angles θ, the alignment of the cell body is quite different over time, predicting different behaviors for free-swimming bacteria due to the changes in velocities shown in Fig. 8.

IV. DISCUSSION AND CONCLUSION

During flick motility, the hook varies in stiffness over two orders of magnitude, which leads to a variety of dynamical behaviors, such as orbits, precession, and unstable deflections. We have studied how these behaviors arise from the linear response, nonlinear response, and large deformations of the hook.

For stiff hooks in orbits with small deflections, the behavior of the hook is linear and the hook can be replaced by more efficient linear bending and spring models. For this regime, errors arising from ignoring hydrodynamic interactions are about 40% on the free-swimming speeds of bacteria. As the hook stiffness decreases, we described critical values where the trajectory of the flagellum transitions to precession.

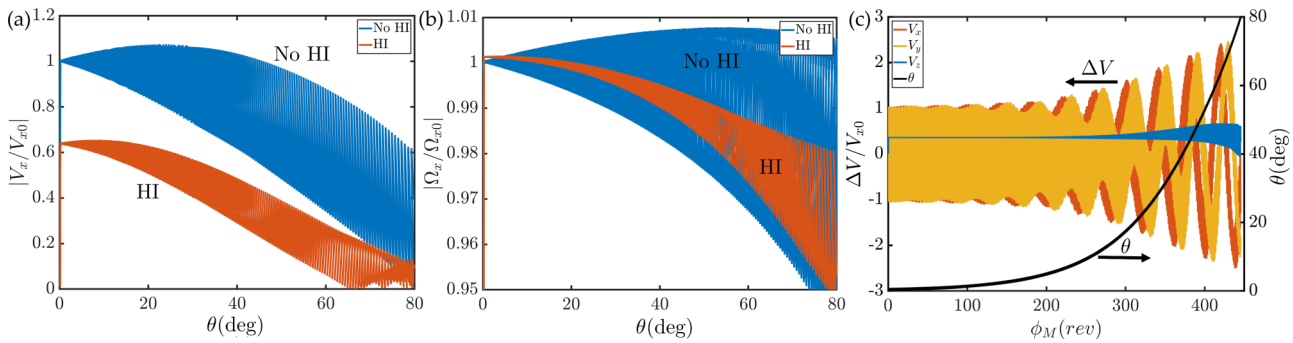

FIG. 8. The effect of hydrodynamic interaction (HI) between the cell body and flagellum on swimming velocities for various deflection angles θ. (a) The velocity along the x axis (swimming direction) normalized by V_{x0}, the velocity at $\theta = 0$ for the noninteracting case. (b) The cell-body angular velocity Ω_x about the swimming direction normalized by Ω_{x0}, the angular velocity at $\theta = 0$ for the noninteracting case. (c) The difference $\Delta V_{x,y,z}$ between velocities with and without hydrodynamic interactions as a function of motor angle ϕ_M during a trajectory. The corresponding deflection angle θ is plotted on the right axis.

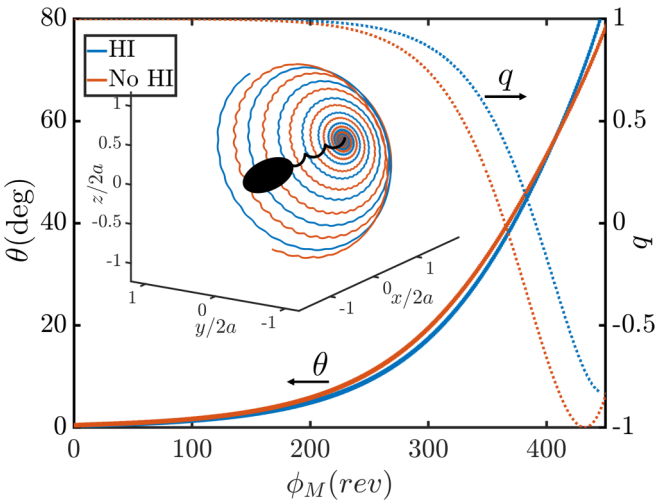

FIG. 9. The effects of hydrodynamic interactions on the swimming dynamics. While the deflection angle θ (solid lines, left axes) is similar with and without hydrodynamic interactions, the instantaneous alignment parameters q of the cell body (dotted lines, right axes) differ due to the cumulative effect of different swimming velocities predicted with and without hydrodynamic interactions. The inset shows trajectories of the flagellum end point with (blue) and without (red) hydrodynamic interactions.

Because the transition still involves small hook deformations, the behavior of the hook is still linear. We identified critical hook stiffnesses k_H^* with flick initiation and compared the critical values to experimental observations. We found that replacing the hook with linear bending and torsional springs predicts the observations well, but the predictions can be improved by considering the hydrodynamic interaction between the cell body, flagellum, and hook.

As the hook stiffness decreases further, we found that nonlinear effects destabilize precession for $k_H < 0.98k_H^*$, producing unstable deflections, while linear models fail to capture this qualitative behavior. However, nonlinear spring models are still quantitatively inaccurate when compared to full Kirchoff rod models since they do not properly capture the twisting behavior of the hook.

For very flexible hooks with $k_H < 0.4$, large deformations of the hook become important and their shapes become complex curves. This range of stiffnesses is important biologically when bacteria reverse to forward motility in short preflick runs. The corresponding large flagellum deflections make hydrodynamic interactions more significant and change the total swimming dynamics.

In conclusion, understanding the flick motility of a free-swimming bacteria requires incorporating different physical phenomena when the stiffness varies widely during flick. For stiff hooks, the critical stiffness at which straight-swimming orbits are destabilized can be predicted by linear models. However, flick motility can involve softer unwound hooks which are more sensitive to the applied load and show very nonlinear dynamics which must be treated accurately in order to obtain the true swimming dynamics of bacteria. To achieve this, a full treatment of the hook dynamics (Kirchhoff rod model and numerical inextensible model) and inclusion of hydrodynamic interactions of the cell body, flagellum, and hook are required to quantitatively simulate flick motility. Note that we do not use a centerline discretization of regularized Stokeslets for the hook and filament in our numerical Kirchhoff rod models. This is due to the fact that centerline regularized Stokeslets [18] have limited resolution in discretization of the hook into segments since Stokeslets have a blob parameter, and hence spacing, of the same order as the filament's diameter [25]. The typical length to diameter ratio of the hook is $L/d \approx 10$ [6], suggesting that centerline regularized Stokeslets would allow only approximately 10 segments, not enough to accurately describe large deformations of the hook [6].

In this paper, we assume rigid flagellar filaments and considered flexible hooks with a constant (in time) stiffness in our simulations. However, since the stiffness of the hook changes as it is wound during flick motility, it is necessary to understand the true hook winding dynamics and stiffness as a function of time in order to understand the whole process of the flick motility. Furthermore, in our previous work [5], we showed that the flexibility of the flagellar filaments could be significant during flick motility because of large loads due to large deflections of the flagellum. Both nonlinear hook effects and flagellum flexibility can destabilize precession independently, but should be combined in future work to accurately model flick motility. For such future work, which combines both the time dependence of hook stiffness and flagellum flexibility, this study suggests that it is most appropriate to use the numerical inextensible model, which can spatially resolve bending of both the hook and flagellum, include time-dependent hook stiffnesses, as well as include all hydrodynamic interactions.

ACKNOWLEDGMENTS

We acknowledge support from Grants No. CBET-1805847 and No. CBET-1651031 (H.C.F.) and the University of Utah Center for High Performance Computing.

APPENDIX A: INEXTENSIBLE KIRCHHOFF ROD MODEL OF HOOK

In this Appendix, we describe the inextensible Kirchhoff rod model following an approach used in our previous paper [5] and a report by Shum *et al.* [17]. The undeformed straight hook of length L_H is in the x direction in the body-fixed frame, connecting the ellipsoidal cell body to a helical flagellum (Fig. 2). The deformed centerline of the hook is defined by a three-dimensional curve $\mathbf{x}(s)$ with an associated orthonormal triad $\{\mathbf{d_1}(s), \mathbf{d_2}(s), \mathbf{d_3}(s)\}$ as a function of the arc length $s \in [0, L_H]$. $\mathbf{d_2}(s)$ and $\mathbf{d_3}(s)$ describe the orientations of the material cross sections and $\mathbf{d_1}(s) = \partial\mathbf{x}/\partial s$ describes the tangent to the centerline.

A cross-sectional force $\mathbf{F}$ and moment $\mathbf{M}$ are exerted by the material with greater s on the material with lesser s. The constitutive law for the moment is

$$\mathbf{M} = GJ\kappa_1\mathbf{d}_1 + EI(\kappa_2\mathbf{d}_2 + \kappa_3\mathbf{d}_3), \tag{A1}$$

where the twist vector $\boldsymbol{\kappa} = \kappa_i(s)\mathbf{d}_i(s)$ measures the local curvature of the rod via $\partial_s\mathbf{d}_i = \boldsymbol{\kappa} \times \mathbf{d}_i$, EI is the bending stiffness

related to Young's modulus E, and GJ is the torsional stiffness of the rod related to shear modulus G. I and J are second moments of the cross-sectional area about the bending or twisting axis, respectively.

The Kirchhoff equations for the force and torque balance are

$$\partial_s \mathbf{F} + \mathbf{f} = \mathbf{0}, \quad \partial_s \mathbf{M} + \mathbf{d}_1 \times \mathbf{F} + \mathbf{m} = \mathbf{0}, \tag{A2}$$

where $\mathbf{f}$ and $\mathbf{m}$ are external hydrodynamic force and torque densities per length, respectively. Ignoring hydrodynamic interactions of the filament with surrounding fluid, we assume $\mathbf{f} = \mathbf{0}$ and $\mathbf{m} = \mathbf{0}$ for the Kirchhoff rod model. Equation (A2) together with Eq. (A1) yield a system of system of Ordinary Differential Equations,

$$\begin{aligned}
\mathbf{d}_i' &= \kappa \times \mathbf{d}_i, \\
\kappa_1' &= 0, \\
\kappa_2' &= -(\mathbf{F} \cdot \mathbf{d}_1) + \kappa_1 \kappa_3 (\Gamma - 1), \\
\kappa_3' &= (\mathbf{F} \cdot \mathbf{d}_2) - \kappa_1 \kappa_2 (\Gamma - 1), \\
\mathbf{x}' &= \mathbf{d}_1,
\end{aligned} \tag{A3}$$

where $(\cdot)' = \partial(\cdot)/\partial s$, and $\Gamma = GJ/EI$ is the ratio of the torsional to bending stiffness. We solve these using a fourth-order Runge-Kutta scheme.

The initial conditions at $s = 0$ are $\mathbf{F}_0$, $\mathbf{M}_0$, and $\mathbf{d}_i^B = \mathbf{d}_i(s = 0)$, $i = 1, 2, 3$. Working in the local frame attached to the cell body as shown in Fig. 2, $\mathbf{d}_1^B = [1, 0, 0]$ is in the x direction, while $\mathbf{d}_2^B = [0, \cos(\phi_M), \sin(\phi_M)]$ and $\mathbf{d}_2^B = [0, -\sin(\phi_M), \cos(\phi_M)]$ are given by the motor angle ϕ_M, where $\omega = \dot{\phi}_M$ is the angular velocity of the motor. The initial torque $\mathbf{M}_0$ can be decomposed into the known motor torque M_M in the $\mathbf{d}_1^B$ direction and two unknown perpendicular components of M_2 and M_3 in the $\mathbf{d}_2^B$ and $\mathbf{d}_3^B$ directions, respectively, as $\mathbf{M}_0 = M_M \mathbf{d}_1^B + M_2 \mathbf{d}_2^B + M_3 \mathbf{d}_3^B$. These perpendicular components are constraint torques which keep the hook perpendicular to the body at the hook-body junction. The rod solutions for the ODEs in Eq. (A3) as the initial conditions vary can be summarized by the nonlinear response function given in Eq. (2).

APPENDIX B: LINEAR AND NONLINEAR BENDING AND TORSIONAL SPRING CONSTANTS

To obtain parameters for linear and nonlinear bending and torsional springs described in Eqs. (5) and (6), we parametrize the hook response given by Eq. (3) for applied torque ratios $M_\perp/M_M$. Without loss of generality and for a given motor torque M_M in the x direction, we consider the case where the nonmotor component of $\mathbf{M}_0$ is in the z direction ($M_3 > 0, M_2 = 0, \phi_T = 0$), as shown in Fig. 2 for zero motor rotation angle $\phi_M = 0$. Thus, the orientation of $\mathbf{d}_1$ [described by (θ, ϕ)] is a function of applied torque M_3/M_M and $k_H = EI/(L_H M_M)$. For a given k_H and axial force of 1 pN in the x direction (a typical value for straight swimming), we find that the hook's end point orientation (θ, ϕ) can be approximated by a linear [Eq. (5)] or nonlinear [Eq. (6)] function of M_3/M_M in the regime experienced by *V. alginolyticus* ($1 < M_M < 4$ pN μm [29], $0.1 < M_3/M_M < 1.1$ during flick motility [5]). The coefficients α_θ, α_ϕ, and β_ϕ for linear bending and torsional spring depend on the given hook parameter k_H as

$$\begin{aligned}
\alpha_\theta &= +0.002/k_H^4 - 0.078/k_H^3 + 0.048/k_H^2 + 0.978/k_H, \\
\alpha_\phi &= -0.021/k_H^4 + 0.111/k_H^3 - 0.084/k_H^2 + 0.026/k_H, \\
\beta_\phi &= 0.5/k_H.
\end{aligned} \tag{B1}$$

In the same way, the coefficients α_θ', β_θ', γ_θ' α_ϕ', β_ϕ', γ_ϕ', and δ_ϕ' for nonlinear bending and torsional spring depend on the given hook parameter k_H as

$$\begin{aligned}
\alpha_\theta' &= +0.025/k_H^4 - 0.191/k_H^3 + 0.279/k_H^2 - 0.107/k_H, \\
\beta_\theta' &= -0.034/k_H^4 + 0.186/k_H^3 - 0.259/k_H^2 + 0.097/k_H, \\
\gamma_\theta' &= +0.011/k_H^4 - 0.092/k_H^3 + 0.058/k_H^2 + 0.976/k_H, \\
\alpha_\phi' &= -0.064/k_H^4 + 0.277/k_H^3 - 0.305/k_H^2 + 0.093/k_H, \\
\beta_\phi' &= +0.045/k_H^4 - 0.166/k_H^3 + 0.225/k_H^2 - 0.066/k_H, \\
\gamma_\phi' &= -0.011/k_H^4 + 0.045/k_H^3 - 0.047/k_H^2 + 0.013/k_H, \\
\delta_\phi' &= 0.5/k_H.
\end{aligned} \tag{B2}$$

The coefficients in Eqs. (B1) and (B2) are plotted in Fig. 10 as a function of $1/k_H$. The corresponding errors for the linear and nonlinear bending and torsional springs are $<14\%$ and $<1.4\%$, respectively, relative to the Kirchoff rod calculation of (θ, ϕ) for the ranges $0 < 1/k_H < 2.5$, where α_θ reaches to its maximum at $k_H \approx 0.4$ (Fig. 10).

APPENDIX C: NUMERICAL INEXTENSIBLE ROD MODEL INTERACTING WITH SURROUNDING FLUID

In the final model, we include hydrodynamic interaction of a slender hook filament with its surrounding fluid medium. Since the typical diameter of hook filament is only 10 nm, assuming circular cross sections, the stretchability ratio, which is the ratio between stretching to bending stiffness, is $EA/EI = 16/d_H^2 = 4 \times 10^4\,(1/\mu\mathrm{m}^2)$, meaning that the hook filaments are almost inextensible [6]. Thus, we can use our numerical inextensible model to obtain swimming dynamics and hook response for a free-swimming bacterium [6]. The details of this model are described in our recent paper [6], but briefly, the centerline [defined by space curve $\mathbf{x}(s)$] of the slender hook filament between the cell body and flagellum is discretized into M straight cylindrical segments of equal length Δs and diameter d_H along its centerline in the x direction. Initially segments are between $M + 1$ material points along the arc length such that $s_m = m\Delta s$, labeled by integer index $m = 0, 1, 2, \ldots, M$. We use half-integer values to specify the center of the cylinders, $s_{m+1/2}$. From the constitutive relations of the Kirchhoff rod [6,30] and assuming $\Gamma = GJ/EI = 1$,we calculate the torque $\mathbf{M}^m$ transmitted between discretized segments,

$$\begin{aligned}
M_i^m &= \frac{EI}{\Delta s}\left[\left(\mathbf{d}_j^{m+1/2} - \mathbf{d}_j^{m-1/2}\right) \cdot \mathbf{d}_k^m\right], \\
\mathbf{M}^m &= \sum_{i=1}^{3} M_i^m \mathbf{d}_i^m,
\end{aligned} \tag{C1}$$

where (i, j, k) is any cyclic permutation of (1,2,3). Equation (C1) and a discrete form of Eqs. (A2) yield the total external

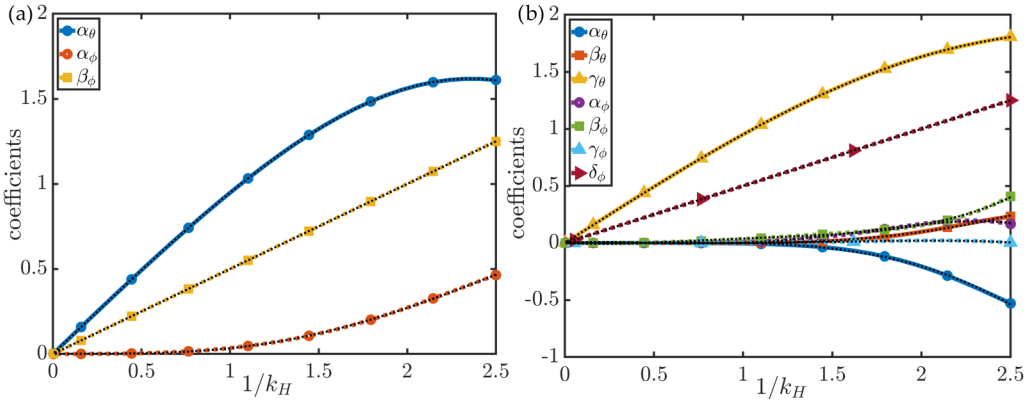

FIG. 10. (a) Coefficients for linear bending and torsional springs [Eq. (B1)] as a function of hook parameter k_H. (b) Coefficients for nonlinear bending and torsional springs [Eq. (B2)] as a function of hook parameter k_H.

force and torque from the surrounding fluid on the center of the segments,

$$\mathbf{M}^{m+1/2} = \mathbf{M}^m - \mathbf{M}^{m+1} - \frac{\Delta s}{2}\left(\mathbf{d}_1^{m+1} \times \mathbf{F}^{m+1} + \mathbf{d}_1^m \times \mathbf{F}^m\right),$$
$$\mathbf{F}^{m+1/2} = \mathbf{F}^m - \mathbf{F}^{m+1}. \tag{C2}$$

Here, $\mathbf{F}^{m+1/2} = \mathbf{f}^{m+1/2}\Delta s$ and $\mathbf{M}^{m+1/2} = \mathbf{m}^{m+1/2}\Delta s$. The force and torque at the free end are zero ($\mathbf{F}^m = \mathbf{0}$, $\mathbf{M}^m = \mathbf{0}$) and the force transmitted between the cross sections at point m can be described by the summation of external forces on segments from the end point to the mth segment as $\mathbf{F}^m = \sum_{i=m}^{M} \mathbf{F}^{m+1/2}$. Note that the total force and torque applied on the cell body are equal to the force and torque at $s = 0$; $\mathbf{F}^c = \mathbf{F}^0$ and $\mathbf{M}^c = \mathbf{M}^0$ satisfy force- and torque-free conditions on the swimmer. Thus, given a configuration at one instant of time, we have $3 + 3M$ knowns (3 components of the cell-body force and $3M$ components of the cross-sectional torques of the segments) after combining these equations.

Next, we couple these calculated torques with hydrodynamic interactions of segments to find translational and rotational velocities of segments. The hydrodynamic interactions are described by the surface boundary element method (BEM) [17,31,32], where the surface of segments is discretized by N equal triangular elements with N_g points on the circular cross sections, the ellipsoidal cell body is triangulated by N_c elements, and the helical flagellar filament is triangulated by N_f elements. By this approach, the translational and rotational velocities of the cell body and segments ($\{\mathbf{V}^{m+1/2}, \boldsymbol{\Omega}^{m+1/2}\}$) are related to the external torques and forces ($\{\mathbf{F}^{m+1/2}, \mathbf{M}^{m+1/2}\}$) through a global resistance matrix $\mathbf{R}$ including all hydrodynamic effects of the triangular elements [6,25]. Although there are $6M$ velocities and angular velocities, the inextensibility of the filament reduces the number of independent velocities to $3 + 3M$, as follows. The inextensibility condition requires that the tangent vector of the centerline is equal to $\mathbf{d}_1$ ($\partial\mathbf{x}/\partial s = \mathbf{d}_1$) and thus $\partial\mathbf{V}/\partial s = \boldsymbol{\Omega}(s) \times \mathbf{d}_1(s)$. In discrete form, this second condition means that the translational velocities at the centers of the segments can be obtained from the translational velocity of the cell body (or, equivalently, the first segment) and all the segment rotational velocities [6]. Thus, we only need to solve for $3 + 3M$ unknowns (3 components of translational velocity of the cell body and $3M$ components of rotational velocity of segments) equal to the number of equations and knowns calculated from cross-sectional torques, as explained above. Integrating the translational and rotational velocities in time, we trace the trajectory of the segments in the local body frame attached to the cell body.

For the numerical analysis, the initially straight hook at $t = 0$ is discretized into 100 uniform cylindrical segments, and for the hydrodynamic interactions, cross sections are discretized by 12 points, leading to 920 triangular boundary elements [32]. We also consider hydrodynamic interactions between the cell body and flagellar filament using the same boundary element method where the surface of the body and rigid flagellum is discretized by 640 and 3200 triangular elements, respectively.

[1] H. C. Berg, Annu. Rev. Biochem. **72**, 19 (2003).
[2] H. C. Berg and L. Turner, Biophys. J. **65**, 2201 (1993).
[3] H. C. Berg and R. A. Anderson, Nature (London) **245**, 380 (1973).
[4] K. Son, J. S. Guasto, and R. Stocker, Nat. Phys. **9**, 494 (2013).
[5] M. Jabbarzadeh and H. C. Fu, Phys. Rev. E **97**, 012402 (2018).
[6] M. Jabbarzadeh and H. C. Fu, J. Comput. Phys. **418**, 109643 (2020).
[7] N. C. Darnton and H. C. Berg, Biophys. J. **92**, 2230 (2007).
[8] F. T. M. Nguyen and M. D. Graham, Phys. Rev. E **98**, 042419 (2018).
[9] M. T. Brown, B. C. Steel, C. Silvestrin, D. A. Wilkinson, N. J. Delalez, C. N. Lumb, B. Obara, J. P. Armitage, and R. M. Berry, J. Bacteriol. **194**, 3495 (2012).
[10] K. Ishimoto and E. Lauga, Proc. Math. Phys. Eng. Sci. **475**, 20180690 (2019).
[11] I. Sporing, V. A. Martinez, C. Hotz, J. Schwarz-Linek, K. L. Grady, J. M. Nava-Sedeño, T. Vissers, H. M. Singer, M. Rohde,

C. Bourquin, H. Hatzikirou, W. C. K. Poon, Y. S. Dufour, and M. Erhardt, PLOS Biol. **16**, e2006989 (2018).
[12] N. Darnton, L. Turner, S. Rojevsky, and H. C. Berg, J. Bacteriol. **189**, 1756 (2007).
[13] L. Xie, T. Altindal, S. Chattopadhyay, and X.-L. Wu, Proc. Natl. Acad. Sci. **108**, 2246 (2011).
[14] F. T. Nguyen and M. D. Graham, Biophys. J. **112**, 1010 (2017).
[15] E. E. Riley, D. Das, and E. Lauga, Sci. Rep. **8**, 10728 (2018).
[16] K. Ishimoto, J. Fluid Mech. **880**, 620 (2019).
[17] H. Shum and E. Gaffney, Phys. Fluids **24**, 061901 (2012).
[18] Y. Park, Y. Kim, and S. Lim, J. Fluid Mech. **859**, 586 (2019).
[19] M. A. Constantino, M. Jabbarzadeh, H. C. Fu, and R. Bansil, Sci. Adv. **2**, e1601661 (2016).
[20] M. A. Constantino, M. Jabbarzadeh, H. C. Fu, Z. Shen, J. G. Fox, F. Haesebrouck, S. K. Linden, and R. Bansil, Sci. Rep. **8**, 14415 (2018).
[21] S. Ahmadvand, M. Elahifard, M. Jabbarzadeh, A. Mirzanejad, K. Pflughoeft, B. Abbasi, and B. Abbasi, J. Phys. Chem. B **123**, 787 (2019).
[22] Y. Hyon, T. R. Powers, R. Stocker, H. C. Fu *et al.*, J. Fluid Mech. **705**, 58 (2012).
[23] K. Samsami, S. A. Mirbagheri, F. Meshkati, and H. C. Fu, Phys. Rev. Fluids **5**, 064202 (2020).
[24] H. C. Fu, M. Jabbarzadeh, and F. Meshkati, Phys. Rev. E **91**, 043011 (2015).
[25] J. Martindale, M. Jabbarzadeh, and H. Fu, Phys. Fluids **28**, 021901 (2016).
[26] R. Cortez, SIAM J. Sci. Comput. **23**, 1204 (2001).
[27] R. Cortez, L. Fauci, and A. Medovikov, Phys. Fluids **17**, 031504 (2005).
[28] Y. Park, Y. Kim, W. Ko, and S. Lim, Phys. Rev. E **95**, 022410 (2017).
[29] Y. Sowa, H. Hotta, M. Homma, and A. Ishijima, J. Mol. Biol. **327**, 1043 (2003).
[30] S. D. Olson, S. Lim, and R. Cortez, J. Comput. Phys. **238**, 169 (2013).
[31] N. Phan-Thien, T. Tran-Cong, and M. Ramia, J. Fluid Mech. **184**, 533 (1987).
[32] M. Jabbarzadeh and H. C. Fu, J. Fluid Mech. **851**, 715 (2018).